

1 **The sequence of human ACE2 is suboptimal for binding 2 the S spike protein of SARS coronavirus 2**

3 **Erik Procko**

4 Department of Biochemistry, University of Illinois, Urbana IL 61801

5 Email: coronavirus-research@illinois.edu

6 **SUMMARY.** The rapid and escalating spread of SARS coronavirus 2 (SARS-CoV-2)
7 poses an immediate public health emergency. The viral spike protein S binds ACE2
8 on host cells to initiate molecular events that release the viral genome
9 intracellularly. Soluble ACE2 inhibits entry of both SARS and SARS-2 coronaviruses
10 by acting as a decoy for S binding sites, and is a candidate for therapeutic,
11 prophylactic and diagnostic development. Using deep mutagenesis, variants of ACE2
12 are identified with increased binding to the receptor binding domain of S. Mutations
13 are found across the interface, in the N90-glycosylation motif, and at buried sites
14 where they are predicted to enhance local folding and presentation of the interaction
15 epitope. When single substitutions are combined, large increases in binding can be
16 achieved. The mutational landscape offers a blueprint for engineering high affinity
17 proteins and peptides that block receptor binding sites on S to meet this
18 unprecedented challenge.

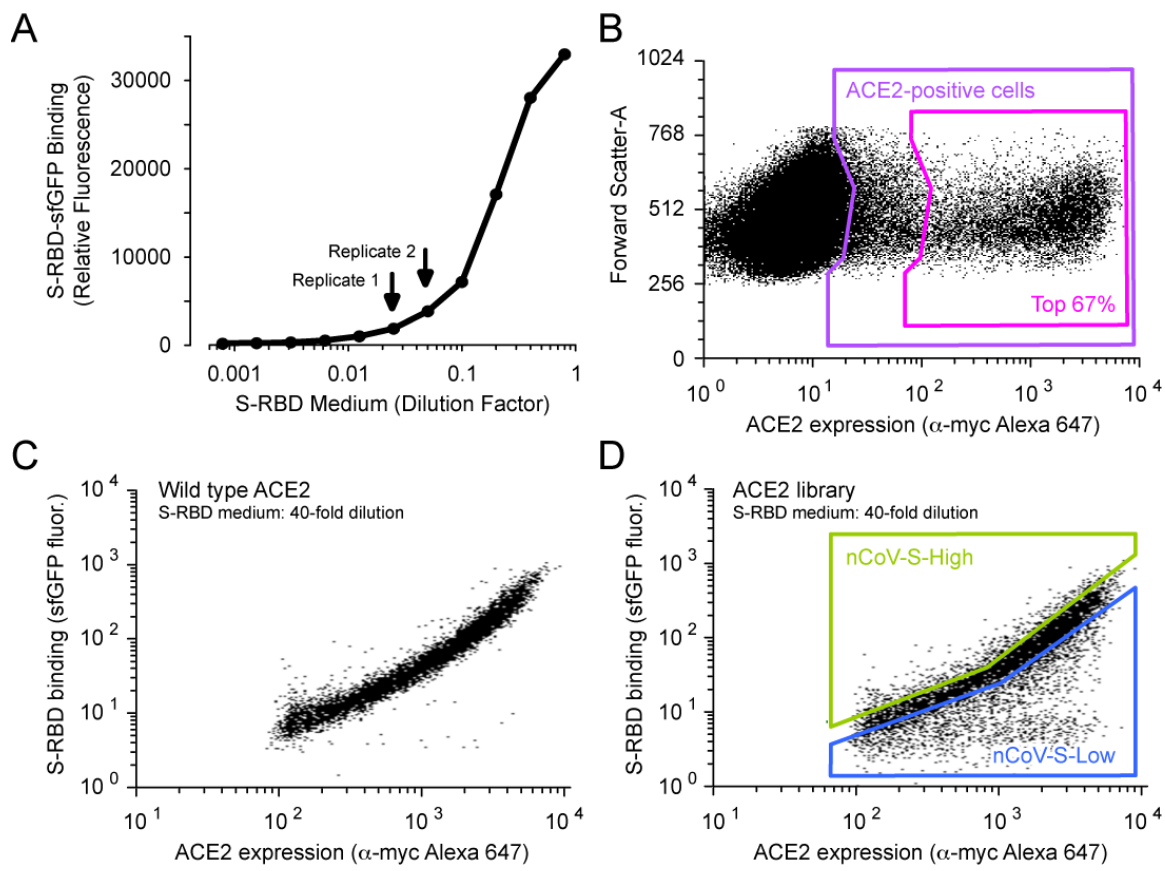
19 In December, 2019, a novel zoonotic betacoronavirus closely related to bat coronaviruses
20 spilled over to humans, possibly at the Huanan Seafood Market in the Chinese city of
21 Wuhan (1, 2). The virus, called SARS-CoV-2 due to its similarities with the severe acute
22 respiratory syndrome (SARS) coronavirus responsible for a smaller outbreak nearly two
23 decades prior (3, 4), has since spread human-to-human rapidly across the world,
24 precipitating extraordinary containment measures from governments (5). These events
25 are unlike any experienced in generations. Symptoms of coronavirus disease 2019 (COVID-
26 19) range from mild to dry cough, fever, pneumonia and death, and SARS-CoV-2 is
27 devastating among the elderly and other vulnerable groups (6, 7).

28 The S spike glycoprotein of SARS-CoV-2 binds angiotensin-converting enzyme 2 (ACE2) on
29 host cells (2, 8-13). S is a trimeric class I viral fusion protein that is proteolytically
30 processed into S1 and S2 subunits that remain noncovalently associated in a prefusion
31 state (8, 11, 14). Upon engagement of ACE2 by a receptor binding domain (RBD) in S1 (15),
32 conformational rearrangements occur that cause S1 shedding, cleavage of S2 by host
33 proteases, and exposure of a fusion peptide adjacent to the S2' proteolysis site (14, 16-18).
34 Favorable folding of S to a post-fusion conformation is coupled to host cell/virus
35 membrane fusion and cytosolic release of viral RNA. Atomic contacts with the RBD are
36 restricted to the protease domain of ACE2 (19, 20), and soluble ACE2 (sACE2) in which the
37 transmembrane domain is removed is sufficient for binding S and neutralizing infection
38 (12, 21-24). In principle, the virus has limited potential to escape sACE2-mediated
39 neutralization without simultaneously decreasing affinity for native ACE2 receptors,
40 thereby attenuating virulence. Furthermore, fusion of sACE2 to the Fc region of human

41 immunoglobulin can provide an avidity boost while recruiting immune effector functions
42 and increasing serum stability, an especially desirable quality if intended for prophylaxis
43 (23, 25), and sACE2 has proven safe in healthy human subjects (26) and patients with lung
44 disease (27). Recombinant sACE2 is being evaluated in a European phase II clinical trial for
45 COVID-19 managed by Apeiron Biologics, and peptide derivatives of ACE2 are also being
46 explored as cell entry inhibitors (28).

47 Since human ACE2 has not evolved to recognize SARS-CoV-2 S, it was hypothesized that
48 mutations may be found that increase affinity for therapeutic and diagnostic applications.
49 The coding sequence of full length ACE2 with an N-terminal c-myc epitope tag was
50 diversified to create a library containing all possible single amino acid substitutions at 117
51 sites spanning the entire interface with S and lining the substrate-binding cavity. S binding
52 is independent of ACE2 catalytic activity (23) and occurs on the outer surface of ACE2 (19,
53 20), whereas angiotensin substrates bind within a deep cleft that houses the active site
54 (29). Substitutions within the substrate-binding cleft of ACE2 therefore act as controls that
55 are anticipated to have minimal impact on S interactions, yet may be useful for engineering
56 out substrate affinity to enhance *in vivo* safety. However, it is important to note that
57 catalytically active protein may have desirable effects for replenishing lost ACE2 activity in
58 COVID-19 patients in respiratory distress (30, 31).

59 The ACE2 library was transiently expressed in human Expi293F cells under conditions that
60 typically yield no more than one coding variant per cell, providing a tight link between
61 genotype and phenotype (32, 33). Cells were then incubated with a subsaturating dilution
62 of medium containing the RBD of SARS-CoV-2 fused C-terminally to superfolder GFP
63 (sfGFP; (34)) (Fig. 1A). Levels of bound RBD-sfGFP correlate with surface expression levels
64 of myc-tagged ACE2 measured by dual color flow cytometry. Compared to cells expressing
65 wild type ACE2 (Fig. 1C), many variants in the ACE2 library fail to bind RBD, while there
66 appeared to be a smaller number of ACE2 variants with higher binding signals (Fig. 1D).
67 Cells expressing ACE2 variants with high or low binding to RBD were collected by
68 fluorescence-activated cell sorting (FACS), referred to as "nCoV-S-High" and "nCoV-S-Low"
69 sorted populations, respectively. During FACS, fluorescence signal for bound RBD-sfGFP
70 continuously declined, requiring the collection gates to be regularly updated to 'chase' the
71 relevant populations. This is consistent with RBD dissociating over hours during the
72 experiment.



73

74 **Figure 1. A selection strategy for ACE2 variants with high binding to the RBD of SARS-
75 CoV-2 S.**

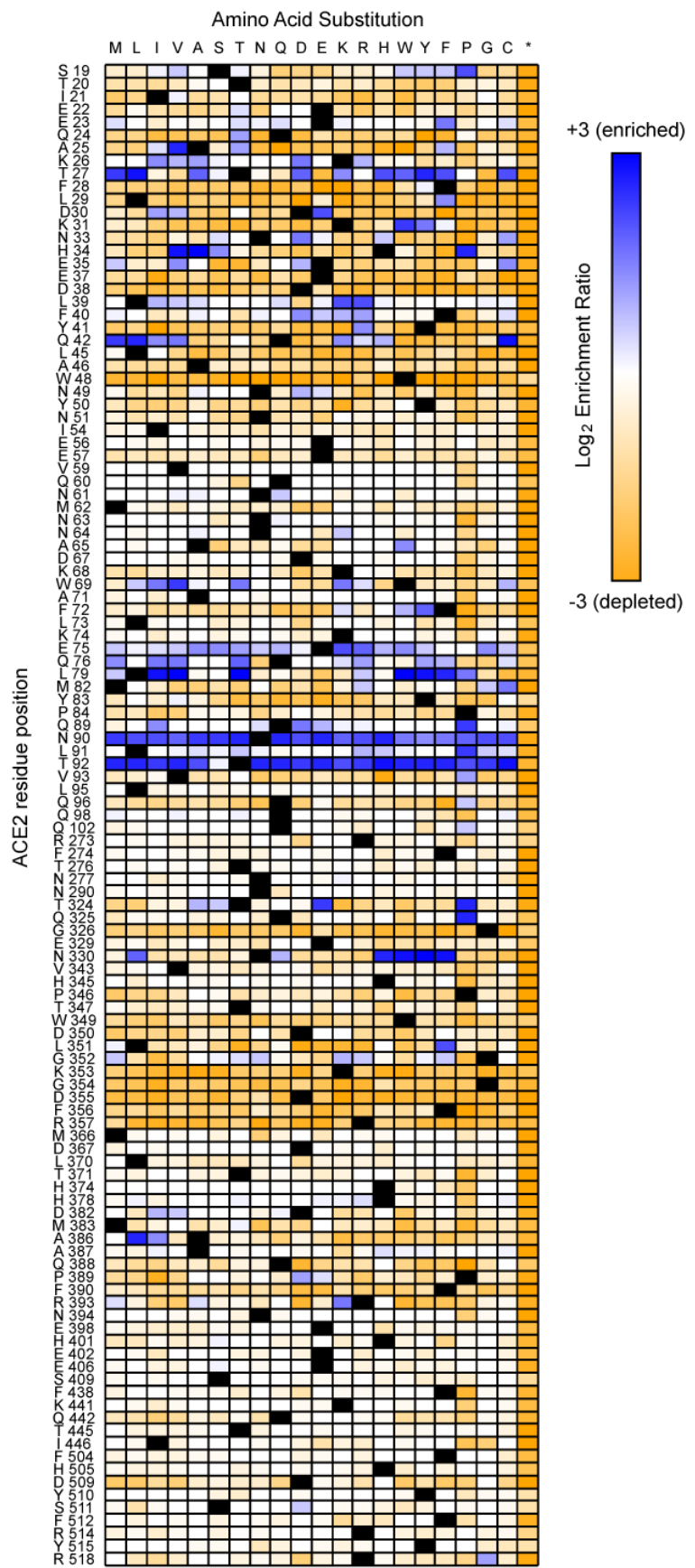
76 (A) Media from Expi293F cells secreting the SARS-CoV-2 RBD fused to sfGFP was collected
77 and incubated at different dilutions with Expi293F cells expressing myc-tagged ACE2. Bound
78 RBD-sfGFP was measured by flow cytometry. The dilutions of RBD-sfGFP-containing medium
79 used for FACS selections are indicated by arrows.

80 (B-C) Expi293F cells were transfected with wild type ACE2 plasmid diluted with a large excess
81 of carrier DNA. It has been previously shown that under these conditions, cells typically acquire
82 no more than one coding plasmid and most cells are negative. Cells were incubated with RBD-
83 sfGFP-containing medium and co-stained with fluorescent anti-myc to detect surface ACE2 by
84 flow cytometry. During analysis, the top 67% (magenta gate) were chosen from the ACE2-
85 positive population (purple gate) (B). Bound RBD was subsequently measured relative to
86 surface ACE2 expression (C).

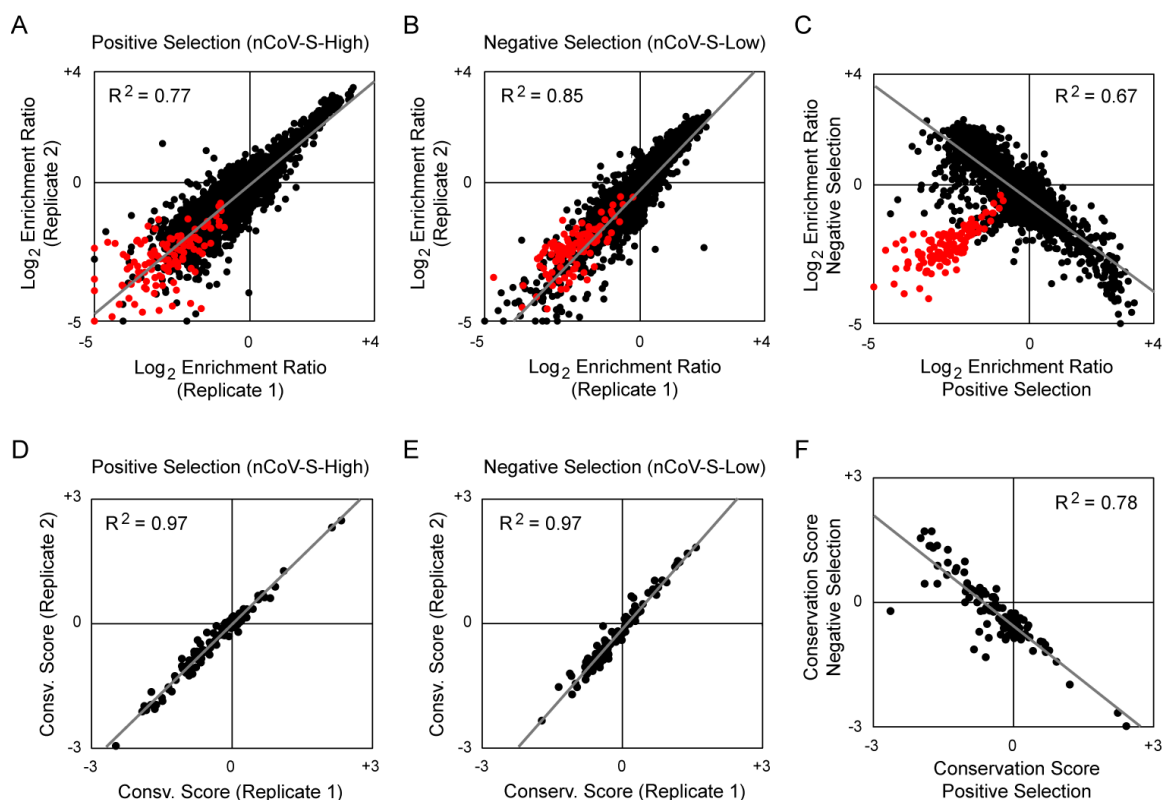
87 (D) Expi293F cells were transfected with an ACE2 single site-saturation mutagenesis library and
88 analyzed as in B. During FACS, the top 15% of cells with bound RBD relative to ACE2
89 expression were collected (nCoV-S-High sort, green gate) and the bottom 20% were collected
90 separately (nCoV-S-Low sort, blue gate).

91 **Figure 2. A mutational landscape of ACE2 for high binding signal to the RBD of SARS-
92 CoV-2 S.**

93 Log₂ enrichment ratios from the nCoV-S-High sorts are plotted from ≤ -3 (i.e.
94 deleterious/deleterious, orange) to neutral (white) to $\geq +3$ (i.e. enriched, dark blue). ACE2 primary
95 structure is on the vertical axis, amino acid substitutions are on the horizontal axis. *, stop
96 codon.



98 Transcripts in the sorted populations were deep sequenced, and frequencies of variants
99 were compared to the naive plasmid library to calculate the enrichment or depletion of all
100 2,340 coding mutations in the library (Fig. 2). This approach of tracking an *in vitro*
101 selection or evolution by deep sequencing is known as deep mutagenesis (35). Enrichment
102 ratios (Fig. 3A and 3B) and residue conservation scores (Fig. 3D and 3E) closely agree
103 between two independent sort experiments, giving confidence in the data. For the most
104 part, enrichment ratios (Fig. 3C) and conservation scores (Fig. 3F) in the nCoV-S-High sorts
105 are anticorrelated with the nCoV-S-Low sorts, with the exception of nonsense mutations
106 which were appropriately depleted from both gates. This indicates that most, but not all,
107 nonsynonymous mutations in ACE2 did not eliminate surface expression. The library is
108 biased towards solvent-exposed residues and has few substitutions of buried hydrophobics
109 that might have bigger effects on plasma membrane trafficking (33).

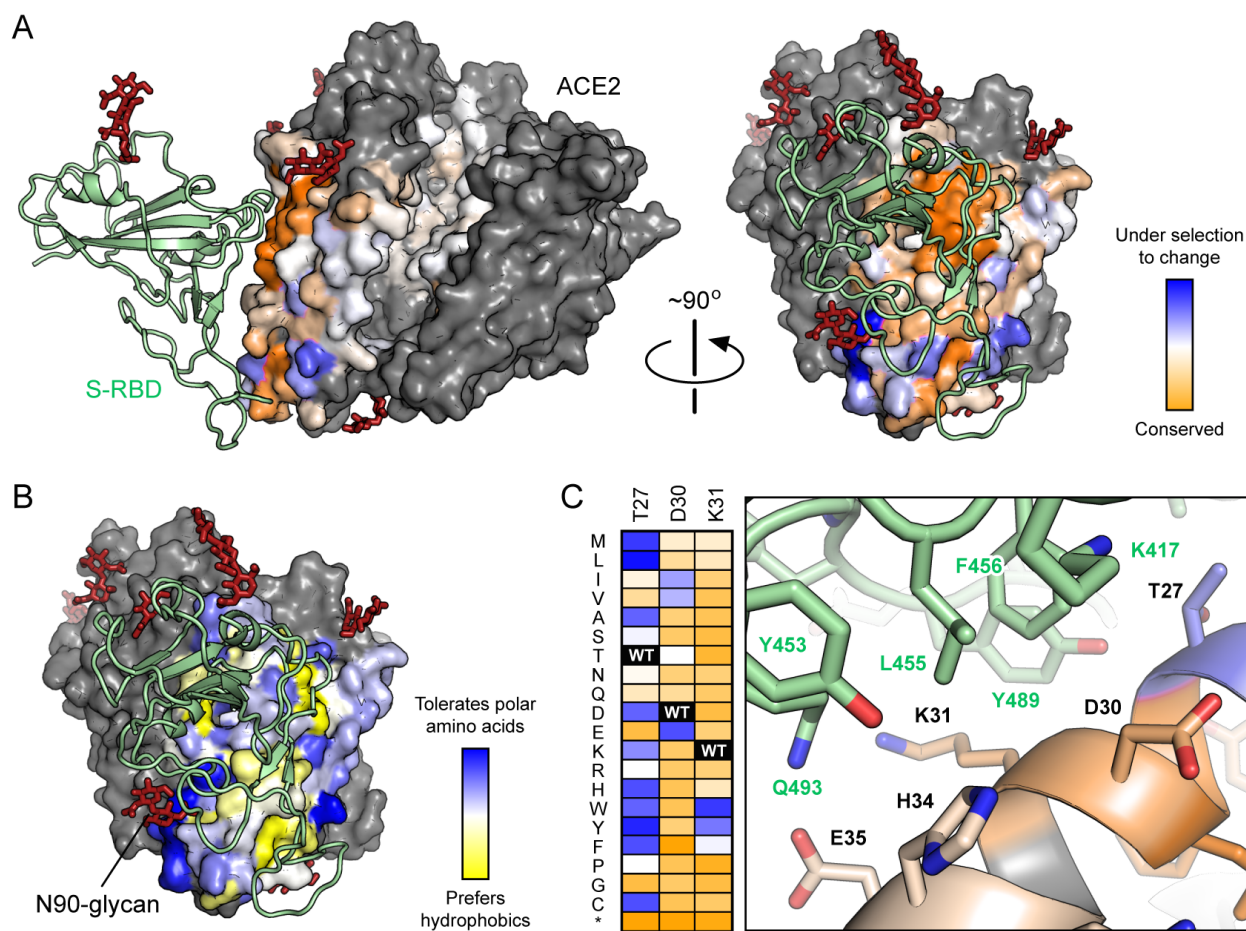


110
111 **Figure 3. Data from independent replicates show close agreement.**
112 **(A-B)** Log₂ enrichment ratios for ACE2 mutations in the nCoV-S-High (A) and nCoV-S-Low (B)
113 sorts closely agree between two independent FACS experiments. Nonsynonymous mutations
114 are black, nonsense mutations are red. Replicate 1 used a 1/40 dilution and replicate 2 used a
115 1/20 dilution of RBD-sfGFP-containing medium. R² values are for nonsynonymous mutations.
116 **(C)** Average log₂ enrichment ratios tend to be anticorrelated between the nCoV-S-High and
117 nCoV-S-Low sorts. Nonsense mutations (red) and a small number of nonsynonymous
118 mutations (black) are not expressed at the plasma membrane and are depleted from both sort
119 populations (i.e. fall below the diagonal).
120 **(D-F)** Correlation plots of residue conservation scores from replicate nCoV-S-High (D) and
121 nCoV-S-Low (E) sorts, and from the averaged data from both nCoV-S-High sorts compared to

122 both nCoV-S-Low sorts (F). Conservation scores are calculated from the mean of the \log_2
123 enrichment ratios for all amino acid substitutions at each residue position.

124 Mapping the experimental conservation scores from the nCoV-S-High sorts to the structure
125 of RBD-bound ACE2 (19) shows that residues buried in the interface tend to be conserved,
126 whereas residues at the interface periphery or in the substrate-binding cleft are
127 mutationally tolerant (Fig. 4A). The region of ACE2 surrounding the C-terminal end of the
128 ACE2 $\alpha 1$ helix and $\beta 3$ - $\beta 4$ strands has a weak tolerance of polar residues, while amino acids
129 at the N-terminal end of $\alpha 1$ and the C-terminal end of $\alpha 2$ prefer hydrophobics (Fig. 4B),
130 likely in part to preserve hydrophobic packing between $\alpha 1$ - $\alpha 2$. These discrete patches
131 contact the globular RBD fold and a long protruding loop of the RBD, respectively.

132 Two ACE2 residues, N90 and T92 that together form a consensus N-glycosylation motif, are
133 notable hot spots for enriched mutations (Fig. 2 and 4A). Indeed, all substitutions of N90
134 and T92, with the exception of T92S which maintains the N-glycan, are highly favorable for
135 RBD binding, and the N90-glycan is thus predicted to partially hinder S/ACE2 interaction.
136 This result may be dependent on the chemical nature of glycan moieties attached in
137 different cell types.



138

139 **Figure 4. Sequence preferences of ACE2 residues for high binding to the RBD of SARS-**
140 **CoV-2 S.**

141 **(A)** Conservation scores from the nCoV-S-High sorts are mapped to the cryo-EM structure
142 (PDB 6M17) of RBD (pale green ribbon) bound ACE2 (surface). The view at left is looking
143 down the substrate-binding cavity, and only a single protease domain is shown for clarity.
144 Residues conserved for high RBD binding are orange; mutationally tolerant residues are pale
145 colors; residues that are hot spots for enriched mutations are blue; and residues maintained as
146 wild type in the ACE2 library are grey. Glycans are dark red sticks.

147 **(B)** Average hydrophobicity-weighted enrichment ratios are mapped to the RBD-bound ACE2
148 structure, with residues tolerant of polar substitutions in blue, while residues that prefer
149 hydrophobic amino acids are yellow.

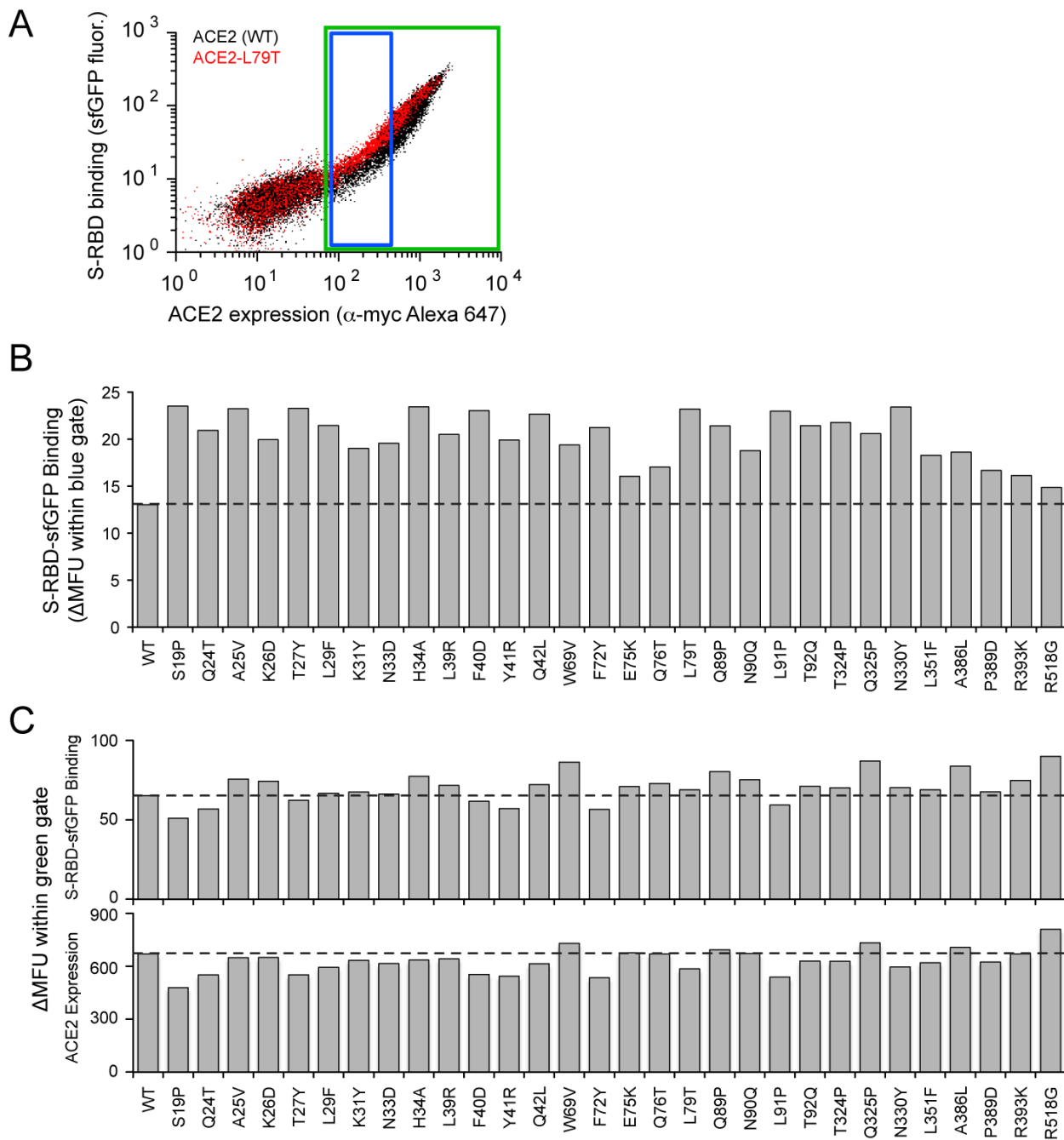
150 **(C)** A magnified view of part of the ACE2 (colored by conservation score as in A) / RBD (pale
151 green) interface. Accompanying heatmap plots \log_2 enrichment ratios from the nCoV-S-High
152 sort for substitutions of ACE2-T27, D30 and K31 from ≤ -3 (depleted) in orange to $\geq +3$
153 (enriched) in dark blue.

154 Mining the data identifies many ACE2 mutations that are enriched for RBD binding. For
155 instance, there are 122 mutations to 35 positions in the library that have \log_2 enrichment
156 ratios >1.5 in the nCoV-S-High sort. By comparing the mutational landscape with human
157 genetic diversity, it has been proposed that ACE2 polymorphisms are relevant to COVID-19
158 pathogenesis and transmission (36, 37), although this will require further validation. At
159 least a dozen ACE2 mutations at the structurally characterized interface enhance RBD
160 binding, and will be useful for engineering highly specific and tight protein or peptide
161 binders of SARS-CoV-2 S. The molecular basis for how some of these mutations enhance
162 RBD binding can be rationalized from the RBD-bound cryo-EM structure (Fig. 4C):
163 hydrophobic substitutions of ACE2-T27 increase hydrophobic packing with aromatic
164 residues of S, ACE2-D30E extends an acidic side chain to reach S-K417, and aromatic
165 substitutions of ACE2-K31 contribute to an interfacial cluster of aromatics. A search for
166 affinity-enhancing mutations in ACE2 using targeted mutagenesis recently identified D30E
167 (38), providing independent confirmation of the methods used here.

168 Attention was also drawn to mutations in the second shell and farther from the interface
169 that do not directly contact S but instead have putative structural roles. For example,
170 proline substitutions were enriched at five library positions (S19, L91, T92, T324 and
171 Q325) where they might entropically stabilize the first turns of helices. Proline was also
172 enriched at H34, where it may enforce the central bulge in α 1. Multiple mutations were
173 also enriched at buried positions where they will change local packing (e.g. A25V, L29F,
174 W69V, F72Y and L351F). The selection of ACE2 variants for high binding signal therefore
175 not only reports on affinity, but also on presentation at the membrane of folded structure
176 recognized by SARS-CoV-2 S. Whether these mutations selectively stabilize a virus-
177 recognized local structure in ACE2 versus the global protein fold is unclear.

178 Thirty single substitutions highly enriched in the nCoV-S-High sort were validated by
179 targeted mutagenesis (Fig. 5). Binding of RBD-sfGFP to full length ACE2 mutants increased
180 compared to wild type, yet improvements were small and most apparent on cells
181 expressing low ACE2 levels (Fig. 5A). Differences in ACE2 expression between the mutants
182 also correlated with total levels of bound RBD-sfGFP (Fig. 5C). To rapidly assess mutations
183 in a format more relevant to therapeutic and diagnostic development, the soluble ACE2
184 protease domain was fused to sfGFP. Expression levels of sACE2-sfGFP were qualitatively

185 evaluated by fluorescence of the transfected cultures (Fig. 6A), and binding of sACE2-sfGFP
186 to full length S expressed at the plasma membrane was measured by flow cytometry (Fig.
187 6B). A single substitution (T92Q) that eliminates the N90 glycan gave a small increase in
188 binding signal (Fig. 6B). Focusing on the most highly enriched substitutions in the selection
189 for S binding that were also spatially segregated to minimize negative epistasis (39),
190 combinations of mutations in sACE2 gave large increases in S binding (Table 1 and Fig. 6B).
191 While this assay only provides relative differences, the combinatorial mutants have
192 enhanced binding by at least an order of magnitude. Unexplored combinations of mutations
193 may have even greater effects.



194

195 **Figure 5. Single amino acid substitutions in ACE2 predicted from the deep mutational
196 scan to increase RBD binding have small effects.**

197 (A) Expi293F cells expressing full length ACE2 were stained with RBD-sfGFP-containing
198 medium and analyzed by flow cytometry. Data are compared between wild type ACE2 (black)
199 and a single mutant (L79T, red). Increased RBD binding is most discernable in cells expressing
200 low levels of ACE2 (blue gate). In this experiment, ACE2 has an extracellular N-terminal myc
201 tag upstream of residue S19 that is used to detect surface expression.

202 (B) RBD-sfGFP binding was measured for 30 single amino acid substitutions in ACE2. Data are
203 GFP mean fluorescence in the low expression gate (blue gate in panel A) with background
204 fluorescence subtracted.

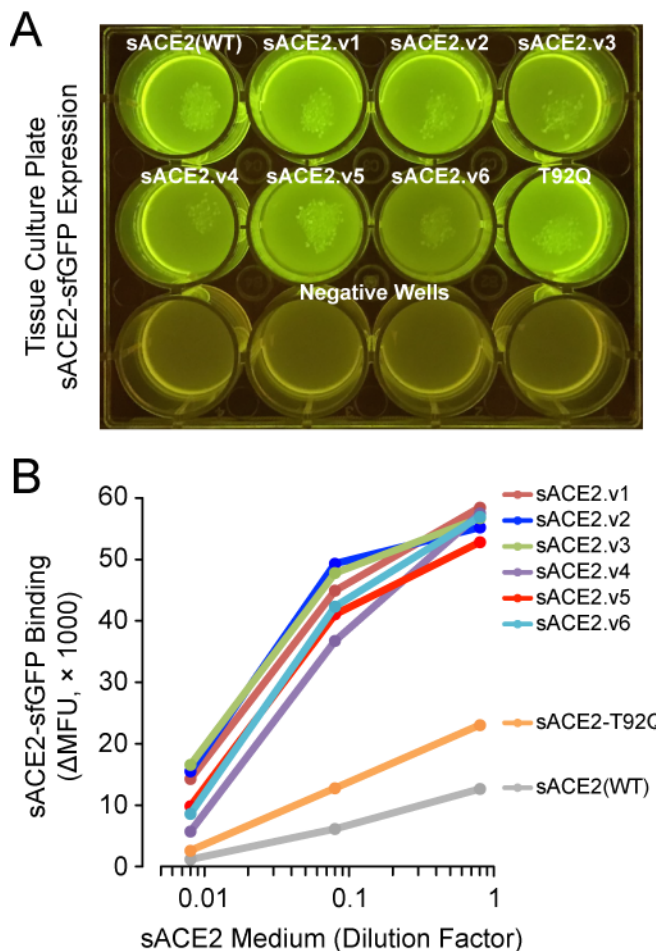
205 (C) RBD-sfGFP binding measured for the total ACE2-positive population (green gate in panel A)
206 is shown in the upper graph, while the lower graph plots ACE2 expression measured by
207 detection of the extracellular myc tag. Total RBD-sfGFP binding correlates with total ACE2
208 expression, and differences in binding between the mutants are therefore most apparent only
209 after controlling for expression levels as in panel A.

210

Table 1. Combinatorial mutants of sACE2.

Variant	Mutations
sACE2.v1	H34A, T92Q, Q325P, A386L
sACE2.v2	T27Y, L79T, N330Y, A386L
sACE2.v2.1	L79T, N330Y, A386L
sACE2.v2.2	T27Y, N330Y, A386L
sACE2.v2.3	T27Y, L79T, A386L
sACE2.v2.4	T27Y, L79T, N330Y
sACE2.v3	A25V, T27Y, T92Q, Q325P, A386L
sACE2.v4	H34A, L79T, N330Y, A386L
sACE2.v5	A25V, T92Q, A386L
sACE2.v6	T27Y, Q42L, L79T, T92Q, Q325P, N330Y, A386L

211

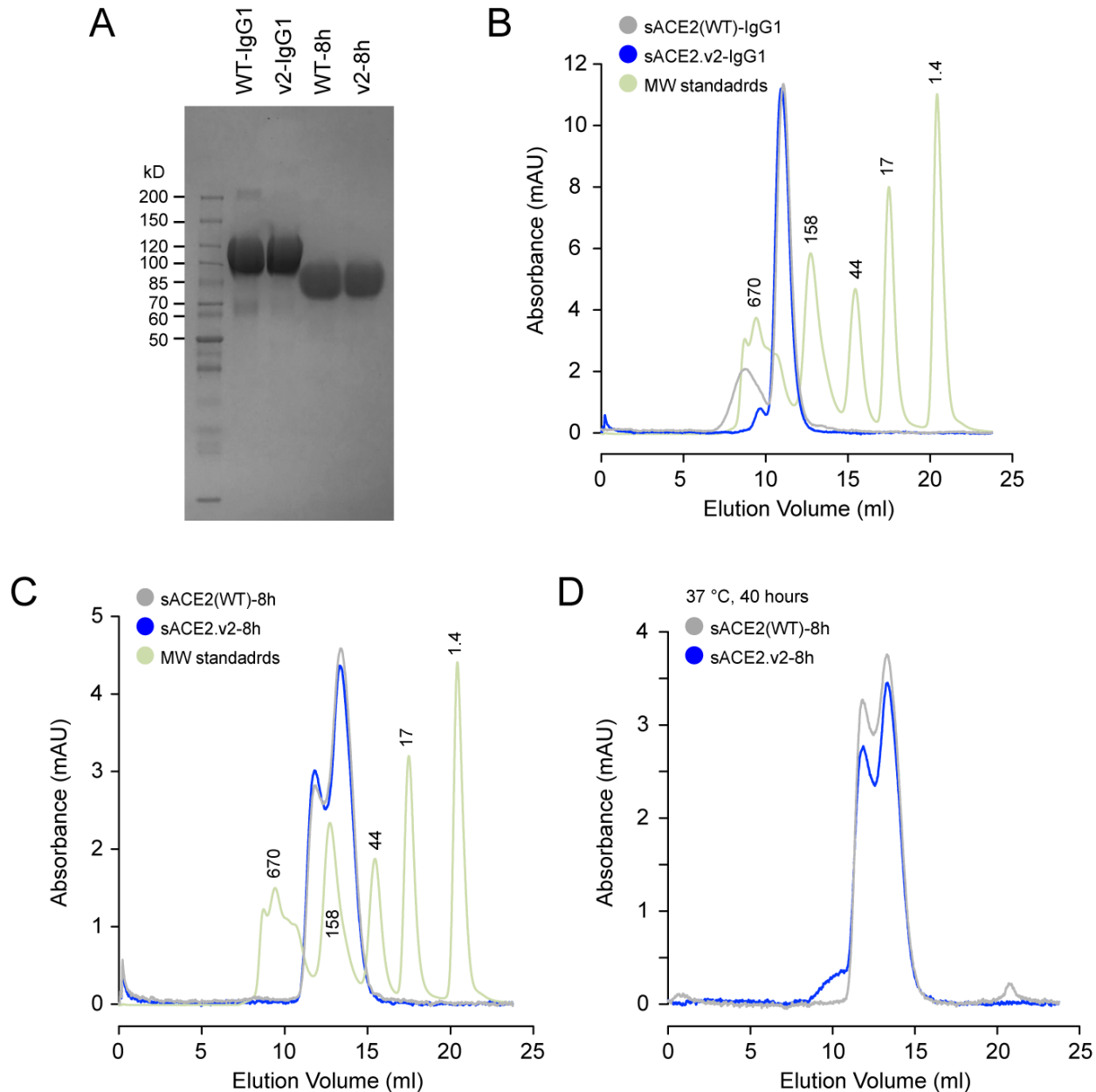


212

213 **Figure 6. Engineered sACE2 with enhanced binding to S.**

214 (A) Expression of sACE2-sfGFP mutants was qualitatively evaluated by fluorescence of the
215 transfected cell cultures.
216 (B) Cells expressing full length S were stained with dilutions of sACE2-sfGFP-containing media
217 and binding was analyzed by flow cytometry.

218 A single variant, sACE2.v2, was chosen for purification and further characterization (Fig. 7).
219 This variant was selected because it was well expressed fused to sfGFP and maintains the
220 N90-glycan, and will therefore present a surface that more closely matches native sACE2 to
221 minimize immunogenicity. The yield of sACE2.v2 was lower than the wild type protein
222 when purified as an 8his-tagged protein (20% lower) or as an IgG1-Fc fusion (60% lower),
223 and by analytical size exclusion chromatography (SEC) a small fraction of sACE2.v2 was
224 found to aggregate after incubation at 37 °C for 40 h (Fig. 7D). Otherwise, sACE2.v2 was
225 indistinguishable from wild type by SEC (Fig. 7C).



226

227 **Figure 7. Analytical SEC of purified sACE2 proteins.**

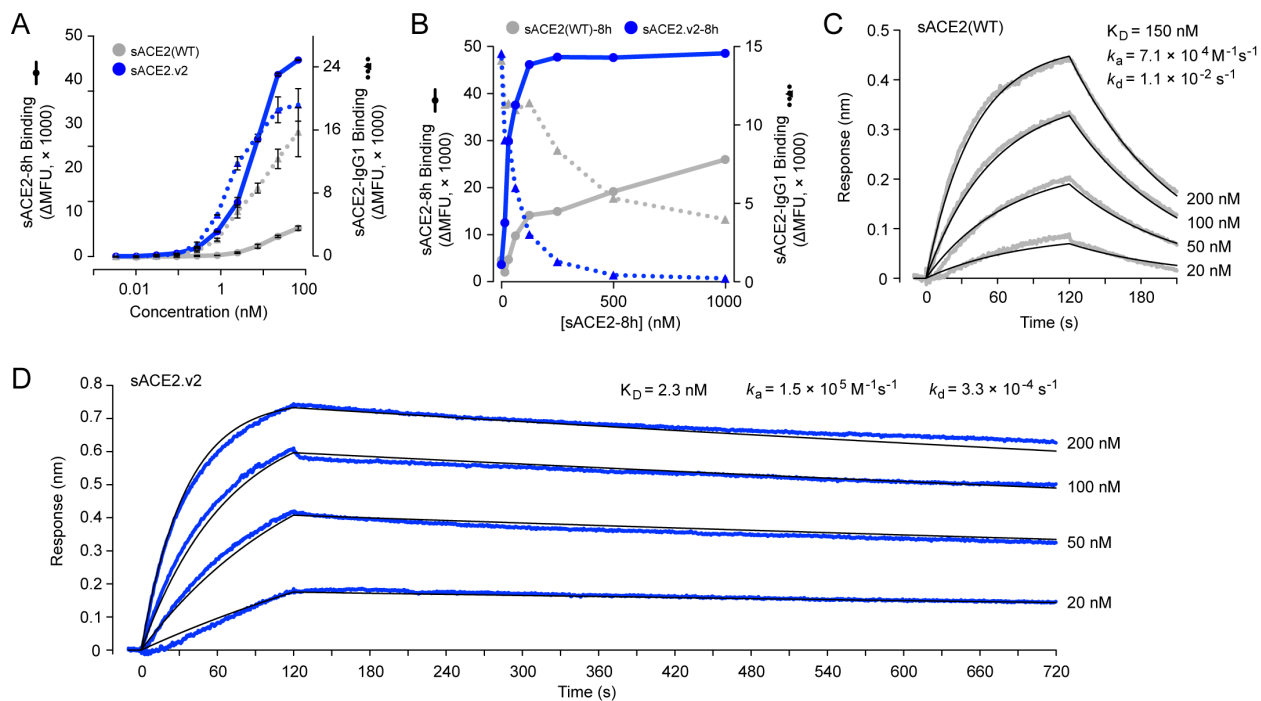
228 **(A)** Purified sACE2 proteins (10 μ g) were separated on a 4-20% SDS-polyacrylamide gel and
229 stained with coomassie.

230 **(B)** Analytical SEC of IgG1-fused wild type sACE2 (grey) and sACE2.v2 (blue). Molecular
231 weights (MW) of standards (green) are indicated in kD above the peaks. Absorbance of the
232 MW standards is scaled for clarity.

233 **(C)** Analytical SEC of 8his-tagged proteins. The major peak corresponds to the expected MW
234 of a monomer. A dimer peak is also observed, although its abundance differs between
235 independent protein preparations (compare to Figure 10D).

236 **(D)** Soluble ACE2-8h proteins were incubated at 37 °C for 40 h and analyzed by SEC.

237 In flow cytometry experiments using purified 8his-tagged sACE2, only sACE2.v2-8h was
 238 found to bind strongly to full length S at the cell surface, suggestive that wild type sACE2
 239 has a high off-rate that causes dissociation during sample washing (Fig. 8A and 9).
 240 Differences between wild type and the variant were less pronounced in the context of an
 241 IgG1-Fc fusion (Fig. 8A and 9), indicating that avidity masks gains in binding of the mutant,
 242 again suggestive that there are off-rate differences between wild type and variant sACE2.
 243 Soluble ACE2.v2-8h outcompetes wild type sACE2-IgG1 for binding to S-expressing cells,
 244 yet wild type sACE2-8h does not outcompete sACE2-IgG1 even at 10-fold higher
 245 concentrations (Fig. 8B). These results align with a study showing that while wild type
 246 sACE2 is highly effective at inhibiting SARS-CoV-2 replication in cell lines and organoids,
 247 extremely high concentrations are required (24). Cell experiments were supported by
 248 biolayer interferometry (BLI), in which IgG1-Fc fused RBD was captured on a biosensor
 249 surface and the association and dissociation kinetics of 8his-tagged sACE2 were
 250 determined. The K_D of wild type sACE2-8h for the RBD was 140 to 150 nM (Fig. 8C and
 251 10F), slightly higher than the K_D values reported by others that range from 1 to 50 nM (8,
 252 10)(40). Variant sACE2.v2 had 65-fold tighter affinity for the RBD, almost entirely due to a
 253 slower off-rate (Fig. 8D). Across all experiments, whether ACE2 is purified as a 8his-tagged
 254 protein or used as a sfGFP-fusion in expression medium, and whether full-length S is
 255 expressed on the plasma membrane or the isolated RBD is immobilized on a biosensor
 256 surface, the characterized sACE2.v2 variant consistently shows one to two orders of
 257 magnitude tighter binding. These experiments support the key discovery from deep
 258 mutagenesis that mutations in human ACE2 exist that increase binding to S of SARS-CoV-2.

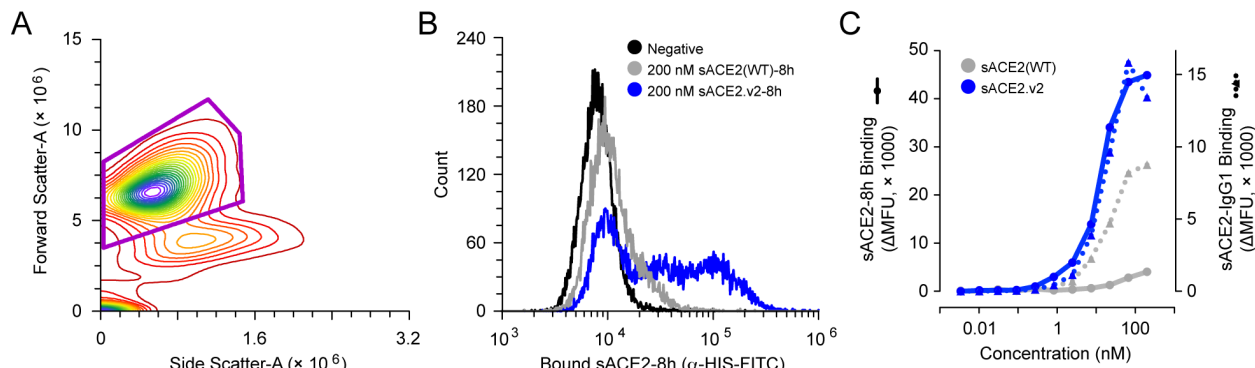


259

260 **Figure 8. A variant of sACE2 with high affinity for S.**

261 (A) Expi293F cells expressing full length S were incubated with purified wild type sACE2 (grey)
 262 or sACE2.v2 (blue) fused to 8his (solid lines) or IgG1-Fc (broken lines). After washing and
 263 staining with secondary antibodies, bound protein was detected by flow cytometry. Data are

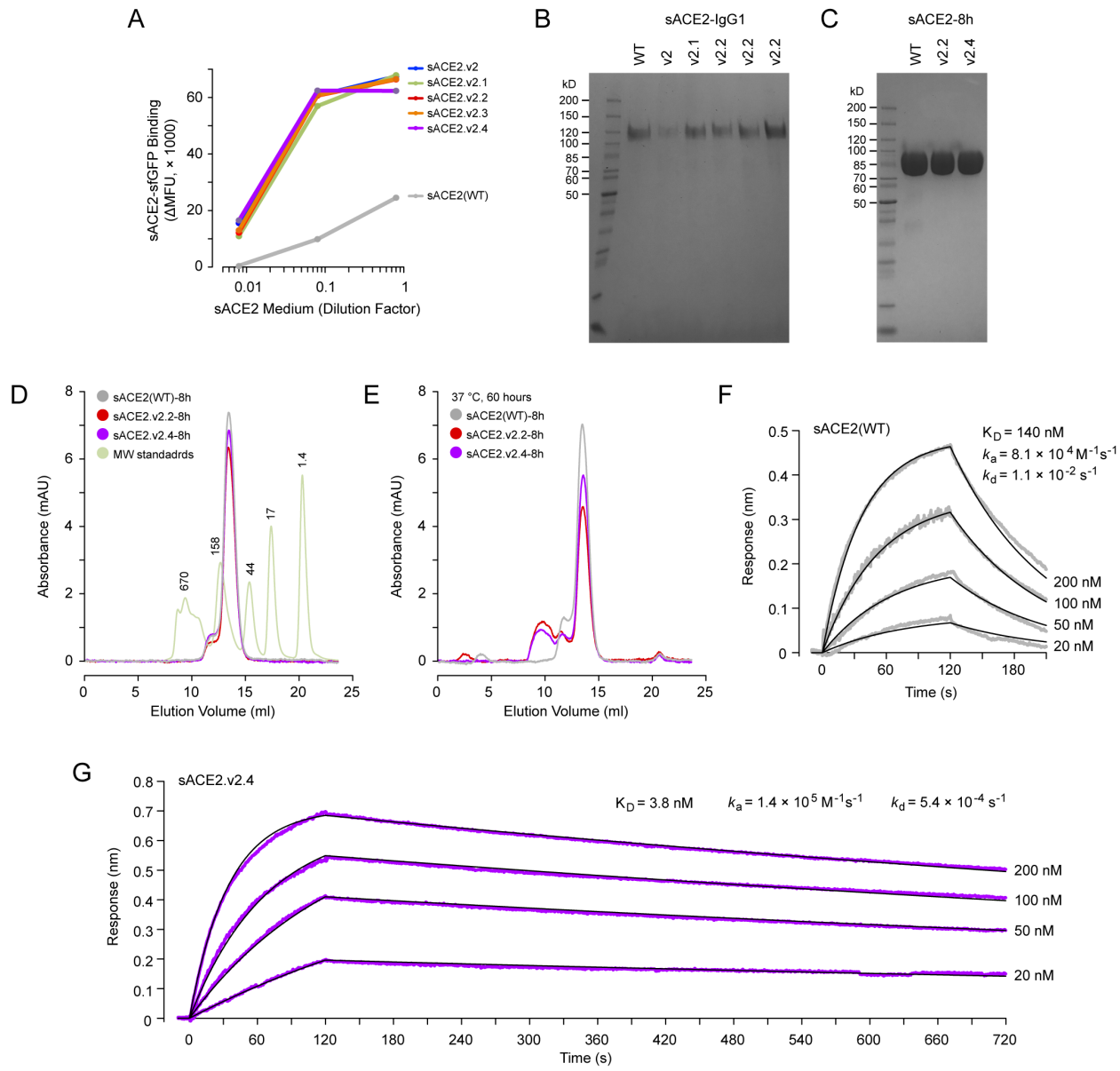
264 mean fluorescence units (MFU) of the total cell population after subtraction of background
265 autofluorescence. n = 2, error bars represent range.
(B) Binding of 100 nM wild type sACE2-IgG1 (broken lines) was competed with wild type
266 sACE2-8h (solid grey line) or sACE2.v2-8h (solid blue line). The competing proteins were
267 added simultaneously to cells expressing full length S, and bound proteins were detected by
268 flow cytometry.
(C) BLI kinetics of wild type sACE2-8h association (t = 0 to 120 s) and dissociation (t > 120 s)
269 with immobilized RBD-IgG1. Compare to an independent protein preparation in Figure 10F.
270 **(D)** Kinetics of sACE2.v2-8h binding to immobilized RBD-IgG1 measured by BLI.
271



273 **Figure 9. Flow cytometry measurements of sACE2 binding to myc-tagged S expressed at
274 the plasma membrane.**

275 **(A)** Expi293F cells expressing full length S, either untagged (Figure 8A) or with an extracellular
276 myc epitope tag (this Figure), were gated by forward-side scattering properties for the main cell
277 population (purple gate).
(B) Histograms showing representative raw data from flow cytometry analysis of myc-S-
278 expressing cells incubated with 200 nM wild type sACE2-8h (grey) or sACE2.v2 (blue). After
279 washing, bound protein was detected with a fluorescent anti-HIS-FITC secondary.
280 Fluorescence of myc-S-expressing cells treated without sACE2 is black.
(C) Binding of purified wild type sACE2 (grey) or sACE2.v2 (blue) fused to 8his (solid lines) or
281 IgG1-Fc (broken lines) to cells expressing myc-S.

282 To address the decreased expression of sACE2.v2, it was hypothesized that the mutational
283 load is too high. Each of the four mutations in sACE2.v2 was reverted back to the wild type
284 identity (Table 1), and binding to full length S at the cell surface was found to remain tight
285 using rapid screening of sACE2-sfGFP-containing expression medium (Fig. 10A).
286 Expression was rescued to varying degrees (Fig. 10B), and one of the variants (sACE2.v2.4
287 with mutations T27Y, L79T and N330Y) was purified with higher yields than wild type
288 (20% and 80% higher for 8his and IgG1-Fc tagged proteins, respectively), although some
289 protein remained aggregated after storage at 37 °C for 60 h (Figure 10D and 10E). A
290 second reversion variant (sACE2.v2.2 with mutations T27Y, N330Y and A386L) has a more
291 hydrophobic surface and higher propensity to partially aggregate after storage at 37 °C,
292 and therefore the partial storage instability may be intrinsically linked to increased
293 hydrophobicity of the mutated ACE2 surface. By BLI, sACE2.v2.4 displayed tight nanomolar
294 binding to the RBD (Fig. 10G), demonstrating that high affinity can be achieved without
295 compromising protein expression and purification. Further sequence optimization focused
296 on whether to include the ACE2 neck domain for stable dimer formation is warranted.
297



300

Figure 10. Optimization of a high affinity sACE2 variant for improved yield.

301 (A) Dilutions of sACE2-sfGFP-containing media were incubated with Expi293F cells expressing
302 full length S. After washing, bound sACE2-sfGFP was analyzed by flow cytometry.
303

304 (B) Coomassie-stained SDS-polyacrylamide gel compares the yield of sACE2-IgG1 variants
305 purified from expression medium by protein A resin.

306 (C) Coomassie-stained gel of purified sACE2-8h variants (10 µg per lane).

307 (D) By analytical SEC, sACE2.v2.2-8h (red) and sACE2.v2.4-8h (purple) are indistinguishable
308 from wild type sACE2-8h (grey). The absorbance of MW standards (green) is scaled for clarity,
309 with MW indicated above the elution peaks in kD.

310 (E) Analytical SEC after storage of the proteins at 37 °C for 60 h.

311 (F) Wild type sACE2-8h association ($t = 0$ to 120 s) and dissociation ($t > 120$ s) with immobilized
312 RBD-IgG1 measured by BLI. Data are comparable to a second independent preparation of
313 sACE2-8h shown in Figure 8C.

314 (G) BLI kinetics of sACE2.v2.4-8h with immobilized RBD-IgG1.

315 While deep mutagenesis of viral proteins in replicating viruses has been extensively
316 pursued to understand escape mechanisms from drugs and antibodies, the work here
317 shows how deep mutagenesis can be directly applicable to anti-viral protein design when
318 the selection method is decoupled from virus replication and focused on host factors.

319 **METHODS**

320 **Plasmids.** The mature polypeptide (a.a. 19-805) of human ACE2 (GenBank NM_021804.1)
321 was cloned in to the NheI-XhoI sites of pCEP4 (Invitrogen) with a N-terminal HA leader
322 (MKTIIIALSYIFCLVFA), myc-tag, and linker (GSPGGA). Soluble ACE2 fused to superfolder
323 GFP (34) was constructed by genetically joining the protease domain (a.a. 1-615) of ACE2
324 to sfGFP (GenBank ASL68970) via a gly/ser-rich linker (GSGGSGSGG), and pasting between
325 the NheI-XhoI sites of pcDNA3.1(+) (Invitrogen). Equivalent sACE2 constructs were cloned
326 with a GSG linker and 8 histidine tag, or a GS linker and the Fc region of IgG1 (a.a. D221-
327 K447). A synthetic human codon-optimized gene fragment (Integrated DNA Technologies)
328 for the RBD (a.a. 333-529) of SARS-CoV-2 S (GenBank YP_009724390.1) was N-terminally
329 fused to a HA leader and C-terminally fused to either superfolder GFP, the Fc region of IgG1
330 or a 8 histidine tag. Assembled DNA fragments were ligated in to the NheI-XhoI sites of
331 pcDNA3.1(+). Human codon-optimized full length S was subcloned from pUC57-2019-
332 nCoV-S(Human) (Molecular Cloud), both untagged (a.a. 1-1273) and with a N-terminal HA
333 leader (MKTIIIALSYIFCLVFA), myc-tag and linker (GSPGGA) upstream of the mature
334 polypeptide (a.a. 16-1273).

335 **Tissue Culture.** Expi293F cells (ThermoFisher) were cultured in Expi293 Expression
336 Medium (ThermoFisher) at 125 rpm, 8 % CO₂, 37 °C. For production of RBD-sfGFP, RBD-
337 IgG1, sACE2-8h and sACE2-IgG1, cells were prepared to 2 × 10⁶ / ml. Per ml of culture, 500
338 ng of plasmid and 3 µg of polyethylenimine (MW 25,000; Polysciences) were mixed in 100
339 µl of OptiMEM (Gibco), incubated for 20 minutes at room temperature, and added to cells.
340 Transfection Enhancers (ThermoFisher) were added 18-23 h post-transfection, and cells
341 were cultured for 4-5 days. Cells were removed by centrifugation at 800 × g for 5 minutes
342 and medium was stored at -20 °C. After thawing and immediately prior to use, remaining
343 cell debris and precipitates were removed by centrifugation at 20,000 × g for 20 minutes.
344 Plasmids for expression of sACE2-sfGFP protein were transfected in to Expi293F cells using
345 Expifectamine (ThermoFisher) according to the manufacturer's directions, with
346 Transfection Enhancers added 22½ h post-transfection, and medium supernatant
347 harvested after 60 h.

348 **Deep mutagenesis.** 117 residues within the protease domain of ACE2 were diversified by
349 overlap extension PCR (41) using primers with degenerate NNK codons. The plasmid
350 library was transfected in to Expi293F cells using Expifectamine under conditions
351 previously shown to typically give no more than a single coding variant per cell (32, 33); 1
352 ng coding plasmid was diluted with 1,500 ng pCEP4-ΔCMV carrier plasmid per ml of cell
353 culture at 2 × 10⁶ / ml, and the medium was replaced 2 h post-transfection. The cells were
354 collected after 24 h, washed with ice-cold PBS supplemented with 0.2 % bovine serum
355 albumin (PBS-BSA), and incubated for 30 minutes on ice with a 1/20 (replicate 1) or 1/40
356 (replicate 2) dilution of medium containing RBD-sfGFP into PBS-BSA. Cells were co-stained

357 with anti-myc Alexa 647 (clone 9B11, 1/250 dilution; Cell Signaling Technology). Cells
358 were washed twice with PBS-BSA, and sorted on a BD FACS Aria II at the Roy J. Carver
359 Biotechnology Center. The main cell population was gated by forward/side scattering to
360 remove debris and doublets, and DAPI was added to the sample to exclude dead cells. Of
361 the myc-positive (Alexa 647) population, the top 67% were gated (Fig. 1B). Of these, the 15
362 % of cells with the highest and 20% of cells with the lowest GFP fluorescence were
363 collected (Fig. 1D) in tubes coated overnight with fetal bovine serum and containing
364 Expi293 Expression Medium. Total RNA was extracted from the collected cells using a
365 GeneJET RNA purification kit (Thermo Scientific), and cDNA was reverse transcribed with
366 high fidelity Accuscript (Agilent) primed with gene-specific oligonucleotides. Diversified
367 regions of ACE2 were PCR amplified as 5 fragments. Flanking sequences on the primers
368 added adapters to the ends of the products for annealing to Illumina sequencing primers,
369 unique barcoding, and for binding the flow cell. Amplicons were sequenced on an Illumina
370 NovaSeq 6000 using a 2×250 nt paired end protocol. Data were analyzed using Enrich (42),
371 and commands are provided in the GEO deposit. Briefly, the frequencies of ACE2 variants in
372 the transcripts of the sorted populations were compared to their frequencies in the naive
373 plasmid library to calculate a \log_2 enrichment ratio and then normalized by the same
374 calculation for wild type. Wild type sequences were neither substantially enriched or
375 depleted, and had \log_2 enrichment ratios of -0.2 to +0.2.

376 **Flow Cytometry Analysis of ACE2-S Binding.** Expi293F cells were transfected with
377 pcDNA3-myc-ACE2, pcDNA3-myc-S or pcDNA3-S plasmids (500 ng DNA per ml of culture
378 at 2×10^6 / ml) using Expifectamine (ThermoFisher). Cells were analyzed by flow
379 cytometry 24 h post-transfection. To analyze binding of RBD-sfGFP to full length myc-
380 ACE2, cells were washed with ice-cold PBS-BSA, and incubated for 30 minutes on ice with a
381 1/30 dilution of medium containing RBD-sfGFP and a 1/240 dilution of anti-myc Alexa 647
382 (clone 9B11, Cell Signaling Technology). Cells were washed twice with PBS-BSA and
383 analyzed on a BD LSR II. To analyze binding of sACE2-sfGFP to full length myc-S, cells were
384 washed with PBS-BSA, and incubated for 30 minutes on ice with a serial dilution of medium
385 containing sACE2-sfGFP and a 1/240 dilution of anti-myc Alexa 647 (clone 9B11, Cell
386 Signaling Technology). Cells were washed twice with PBS-BSA and analyzed on a BD
387 Accuri C6, with the entire Alexa 647-positive population gated for analysis. To measure
388 binding of sACE2-IgG1 or sACE2-8h, myc-S or S transfected cells were washed with PBS-
389 BSA and incubated for 30 minutes with the indicated concentrations of purified sACE2 in
390 PBS-BSA. Cells were washed twice, incubated with secondary antibody (1/100 dilution of
391 chicken anti-HIS-FITC polyclonal from Immunology Consultants Laboratory; or 1/250 anti-
392 human IgG-APC clone HP6017 from BioLegend) for 30 minutes on ice, washed twice again,
393 and fluorescence of the total population after gating by FSC-SSC to exclude debris was
394 measured on a BD Accuri C6. Data were processed with FCS Express (De Novo Software)
395 or BD Accuri C6 Software.

396 **Purification of IgG1-Fc fused proteins.** Cleared expression medium was incubated with
397 KANEKA KanCapA 3G Affinity sorbent (Pall; equilibrated in PBS) for 90 minutes at 4 °C.
398 The resin was collected on a chromatography column, washed with 12 column volumes
399 (CV) PBS, and protein eluted with 5 CV 60 mM Acetate pH 3.7. The eluate was immediately
400 neutralized with 1 CV of 1 M Tris pH 9.0, and concentrated with a 100 kD MWCO

401 centrifugal device (Sartorius). Protein was separated on a Superdex 200 Increase 10/300
402 GL column (GE Healthcare Life Sciences) with PBS as the running buffer. Peak fractions
403 were pooled, concentrated to ~10 mg/ml with excellent solubility, and stored at -80 °C
404 after snap freezing in liquid nitrogen. Protein concentrations were determined by
405 absorbance at 280 nm using calculated extinction coefficients for monomeric, mature
406 polypeptide sequences.

407 **Purification of 8his-tagged proteins.** HisPur Ni-NTA resin (Thermo Scientific)
408 equilibrated in PBS was incubated with cleared expression medium for 90 minutes at 4 °C.
409 The resin was collected on a chromatography column, washed with 12 column volumes
410 (CV) PBS, and protein eluted with a step elution of PBS supplemented with 20 mM, 50 mM
411 and 250 mM imidazole pH 8 (6 CV of each fraction). The 50 mM and 250 mM imidazole
412 fractions were concentrated with a 30 kD MWCO centrifugal device (MilliporeSigma).
413 Protein was separated on a Superdex 200 Increase 10/300 GL column (GE Healthcare Life
414 Sciences) with PBS as the running buffer. Peak fractions were pooled, concentrated to ~5
415 mg/ml with excellent solubility, and stored at -80 °C after snap freezing in liquid nitrogen.

416 **Analytical SEC.** Proteins (200 µl at 2 µM) were separated on a Superdex 200 Increase
417 10/300 GL column (GE Healthcare Life Sciences) equilibrated in PBS. MW standards were
418 from Bio-Rad.

419 **Biolayer Interferometry.** Hydrated anti-human IgG Fc biosensors (Molecular Devices)
420 were dipped in expression medium containing RBD-IgG1 for 60 s. Biosensors with
421 captured RBD were washed in assay buffer, dipped in the indicated concentrations of
422 sACE2-8h protein, and returned to assay buffer to measure dissociation. Data were
423 collected on a BLItz instrument and analyzed with a 1:1 binding model using BLItz Pro Data
424 Analysis Software (Molecular Devices). The assay buffer was 10 mM HEPES pH 7.6, 150
425 mM NaCl, 3 mM EDTA, 0.05% polysorbate 20, 0.5% non-fat dry milk (Bio-Rad).

426 **Reagent and data availability.** Plasmids are deposited with Addgene under IDs 141183-5,
427 145145-78, 149268-71 and 149663-8. Raw and processed deep sequencing data are
428 deposited in NCBI's Gene Expression Omnibus (GEO) with series accession no. GSE147194.

429 **ACKNOWLEDGEMENTS.** Staff at the UIUC Roy J. Carver Biotechnology Center assisted with
430 FACS and Illumina sequencing. Hannah Choi and Krishna Narayanan (University of Illinois)
431 assisted with plasmid preparation. Kui Chan (Orthogonal Biologics Inc) helped characterize
432 sACE2.v2.4. The development of deep mutagenesis to study virus-receptor interactions was
433 supported by NIH award R01AI129719.

434 **CONFLICT OF INTEREST STATEMENT.** E.P. is the inventor on a provisional patent filing
435 by the University of Illinois claiming mutations in ACE2 described here that enhance
436 binding to S. E.P. is a cofounder of Orthogonal Biologics Inc, which has a license from the
437 University of Illinois.

438 **REFERENCES**

- 439 1. N. Zhu *et al.*, A Novel Coronavirus from Patients with Pneumonia in China, 2019. *N.*

- 440 *Engl. J. Med.* **382**, 727–733 (2020).
- 441 2. P. Zhou *et al.*, A pneumonia outbreak associated with a new coronavirus of probable
442 bat origin. *Nature*. **579**, 270–273 (2020).
- 443 3. J. S. M. Peiris *et al.*, Coronavirus as a possible cause of severe acute respiratory
444 syndrome. *Lancet*. **361**, 1319–1325 (2003).
- 445 4. Coronaviridae Study Group of the International Committee on Taxonomy of Viruses,
446 The species Severe acute respiratory syndrome-related coronavirus: classifying
447 2019-nCoV and naming it SARS-CoV-2. *Nat Microbiol*. **4**, 3 (2020).
- 448 5. A. Patel, D. B. Jernigan, 2019-nCoV CDC Response Team, Initial Public Health
449 Response and Interim Clinical Guidance for the 2019 Novel Coronavirus Outbreak -
450 United States, December 31, 2019–February 4, 2020. *MMWR Morb. Mortal. Wkly. Rep.*
451 **69**, 140–146 (2020).
- 452 6. W. Wang, J. Tang, F. Wei, Updated understanding of the outbreak of 2019 novel
453 coronavirus (2019-nCoV) in Wuhan, China. *J. Med. Virol.* **92**, 441–447 (2020).
- 454 7. C. Huang *et al.*, Clinical features of patients infected with 2019 novel coronavirus in
455 Wuhan, China. *Lancet*. **395**, 497–506 (2020).
- 456 8. A. C. Walls *et al.*, Structure, Function, and Antigenicity of the SARS-CoV-2 Spike
457 Glycoprotein. *Cell* (2020), doi:10.1016/j.cell.2020.02.058.
- 458 9. Y. Wan, J. Shang, R. Graham, R. S. Baric, F. Li, Receptor recognition by novel
459 coronavirus from Wuhan: An analysis based on decade-long structural studies of
460 SARS. *J. Virol.* (2020), doi:10.1128/JVI.00127-20.
- 461 10. D. Wrapp *et al.*, Cryo-EM structure of the 2019-nCoV spike in the prefusion
462 conformation. *Science*, eabb2507 (2020).
- 463 11. M. Hoffmann *et al.*, SARS-CoV-2 Cell Entry Depends on ACE2 and TMPRSS2 and Is
464 Blocked by a Clinically Proven Protease Inhibitor. *Cell* (2020),
465 doi:10.1016/j.cell.2020.02.052.
- 466 12. W. Li *et al.*, Angiotensin-converting enzyme 2 is a functional receptor for the SARS
467 coronavirus. *Nature*. **426**, 450–454 (2003).
- 468 13. M. Letko, A. Marzi, V. Munster, Functional assessment of cell entry and receptor
469 usage for SARS-CoV-2 and other lineage B betacoronaviruses. *Nat Microbiol*. **11**, 1860
470 (2020).
- 471 14. M. A. Tortorici, D. Veesler, Structural insights into coronavirus entry. *Adv. Virus Res.*
472 **105**, 93–116 (2019).
- 473 15. S. K. Wong, W. Li, M. J. Moore, H. Choe, M. Farzan, A 193-amino acid fragment of the

- 474 SARS coronavirus S protein efficiently binds angiotensin-converting enzyme 2. *J. Biol.*
475 *Chem.* **279**, 3197–3201 (2004).
- 476 16. I. G. Madu, S. L. Roth, S. Belouzard, G. R. Whittaker, Characterization of a highly
477 conserved domain within the severe acute respiratory syndrome coronavirus spike
478 protein S2 domain with characteristics of a viral fusion peptide. *J. Virol.* **83**, 7411–
479 7421 (2009).
- 480 17. A. C. Walls *et al.*, Tectonic conformational changes of a coronavirus spike
481 glycoprotein promote membrane fusion. *Proc. Natl. Acad. Sci. U.S.A.* **114**, 11157–
482 11162 (2017).
- 483 18. J. K. Millet, G. R. Whittaker, Host cell entry of Middle East respiratory syndrome
484 coronavirus after two-step, furin-mediated activation of the spike protein. *Proc. Natl.*
485 *Acad. Sci. U.S.A.* **111**, 15214–15219 (2014).
- 486 19. R. Yan *et al.*, Structural basis for the recognition of the SARS-CoV-2 by full-length
487 human ACE2. *Science*, eabb2762 (2020).
- 488 20. F. Li, W. Li, M. Farzan, S. C. Harrison, Structure of SARS coronavirus spike receptor-
489 binding domain complexed with receptor. *Science*. **309**, 1864–1868 (2005).
- 490 21. H. Hofmann *et al.*, Susceptibility to SARS coronavirus S protein-driven infection
491 correlates with expression of angiotensin converting enzyme 2 and infection can be
492 blocked by soluble receptor. *Biochem. Biophys. Res. Commun.* **319**, 1216–1221
493 (2004).
- 494 22. C. Lei *et al.*, Potent neutralization of 2019 novel coronavirus by recombinant ACE2-Ig.
495 *bioRxiv*, 2020.02.01.929976 (2020).
- 496 23. M. J. Moore *et al.*, Retroviruses pseudotyped with the severe acute respiratory
497 syndrome coronavirus spike protein efficiently infect cells expressing angiotensin-
498 converting enzyme 2. *J. Virol.* **78**, 10628–10635 (2004).
- 499 24. V. Monteil *et al.*, Inhibition of SARS-CoV-2 infections in engineered human tissues
500 using clinical-grade soluble human ACE2. *Cell*. DOI: **10.1016/j.cell.2020.04.004**, 1–
501 28 (2020).
- 502 25. P. Liu *et al.*, Novel ACE2-Fc chimeric fusion provides long-lasting hypertension
503 control and organ protection in mouse models of systemic renin angiotensin system
504 activation. *Kidney Int.* **94**, 114–125 (2018).
- 505 26. M. Haschke *et al.*, Pharmacokinetics and pharmacodynamics of recombinant human
506 angiotensin-converting enzyme 2 in healthy human subjects. *Clin Pharmacokinet.* **52**,
507 783–792 (2013).
- 508 27. A. Khan *et al.*, A pilot clinical trial of recombinant human angiotensin-converting

- 509 enzyme 2 in acute respiratory distress syndrome. *Crit Care.* **21**, 234 (2017).
- 510 28. G. Zhang, S. Pomplun, A. R. Loftis, A. Loas, B. L. Pentelute, The first-in-class peptide
511 binder to the SARS-CoV-2 spike protein. *bioRxiv*, 2020.03.19.999318 (2020).
- 512 29. P. Towler *et al.*, ACE2 X-ray structures reveal a large hinge-bending motion
513 important for inhibitor binding and catalysis. *J. Biol. Chem.* **279**, 17996–18007
514 (2004).
- 515 30. R. L. Kruse, Therapeutic strategies in an outbreak scenario to treat the novel
516 coronavirus originating in Wuhan, China. *F1000Res.* **9**, 72 (2020).
- 517 31. H. Zhang, J. M. Penninger, Y. Li, N. Zhong, A. S. Slutsky, Angiotensin-converting
518 enzyme 2 (ACE2) as a SARS-CoV-2 receptor: molecular mechanisms and potential
519 therapeutic target. *Intensive Care Med.* **309**, 1864 (2020).
- 520 32. J. D. Heredia *et al.*, Mapping Interaction Sites on Human Chemokine Receptors by
521 Deep Mutational Scanning. *J. Immunol.* **200**, ji1800343–3839 (2018).
- 522 33. J. Park *et al.*, Structural architecture of a dimeric class C GPCR based on co-trafficking
523 of sweet taste receptor subunits. *Journal of Biological Chemistry.* **294**, 4759–4774
524 (2019).
- 525 34. J.-D. Pédelacq, S. Cabantous, T. Tran, T. C. Terwilliger, G. S. Waldo, Engineering and
526 characterization of a superfolder green fluorescent protein. *Nat. Biotechnol.* **24**, 79–
527 88 (2006).
- 528 35. D. M. Fowler, S. Fields, Deep mutational scanning: a new style of protein science. *Nat.*
529 *Methods.* **11**, 801–807 (2014).
- 530 36. E. W. Stawiski *et al.*, Human ACE2 receptor polymorphisms predict SARS-CoV-2
531 susceptibility. *bioRxiv*, 2020.04.07.024752 (2020).
- 532 37. W. T. Gibson, D. M. Evans, J. An, S. J. Jones, ACE 2 Coding Variants: A Potential X-linked
533 Risk Factor for COVID-19 Disease. *bioRxiv*, 2020.04.05.026633 (2020).
- 534 38. Y. Li *et al.*, Potential host range of multiple SARS-like coronaviruses and an improved
535 ACE2-Fc variant that is potent against both SARS-CoV-2 and SARS-CoV-1. *bioRxiv*,
536 2020.04.10.032342 (2020).
- 537 39. J. D. Heredia, J. Park, H. Choi, K. S. Gill, E. Prock, Conformational Engineering of HIV-
538 1 Env Based on Mutational Tolerance in the CD4 and PG16 Bound States. *J. Virol.* **93**,
539 e00219–19 (2019).
- 540 40. J. Shang *et al.*, Structural basis of receptor recognition by SARS-CoV-2. *Nature.* **382**,
541 1199 (2020).
- 542 41. E. Prock *et al.*, Computational design of a protein-based enzyme inhibitor. *J. Mol.*

- 543 *Biol.* **425**, 3563–3575 (2013).
- 544 42. D. M. Fowler, C. L. Araya, W. Gerard, S. Fields, Enrich: software for analysis of protein
545 function by enrichment and depletion of variants. *Bioinformatics*. **27**, 3430–3431
546 (2011).

547